Nano Research 2015, 8(5): 1718–1728
DOI 10.1007/s12274-014-0675-9
Research Article
ISSN 1998-0124
CN 11-5974/O4

Facile production of ultrathin graphitic carbon nitride nanoplatelets for efficient visible-light water splitting

Qing Han, Fei Zhao, Chuangang Hu, Lingxiao Lv, Zhipan Zhang (✉), Nan Chen, and Liangti Qu (✉)

Key Laboratory of Cluster Science, Ministry of Education of China, Beijing Key Laboratory of Photoelectronic/Electrophotonic Conversion Materials, School of Chemistry, Beijing Institute of Technology, Beijing 100081, China

Received: 10 September 2014
Revised: 27 November 2014
Accepted: 1 December 2014

KEYWORDS
ultrathin graphitic carbon nitride nanoplatelets,
eco-friendly,
photocatalyst,
hydrogen production,
visible-light water splitting

ABSTRACT

Ultrathin graphitic carbon nitride nanoplatelets (UGCNPs) are synthesized by a facile manner via an efficient and eco-friendly ball milling approach. The obtained UGCNPs are 2–6 nm in size and 0.35–0.7 nm in thickness, with improved specific surface area over that of bulk graphitic carbon nitride. Photochemical experiments show that the UGCNPs are highly active in visible-light water splitting, with a hydrogen evolution rate of 1,365 $\mu mol \cdot h^{-1} \cdot g^{-1}$, which is 13.7-fold greater than that of their bulk counterparts. The notable improvement in the hydrogen evolution rate observed with UGCNPs under visible light is due to the synergistic effects derived from the increased specific surface area, reduced thickness, and a negative shift in the conduction band concomitant with the exfoliation of bulk graphitic carbon nitride into UGCNPs. In addition to metal-free visible-light-driven photocatalytic hydrogen production, the UGCNPs find attractive applications in biomedical imaging and optoelectronics because of their superior luminescence characteristics.

1 Introduction

With the depletion of fossil fuels and increasing concerns over pollution issues associated with their consumption, there is an urgent need for the development of highly efficient photocatalysts that convert solar energy into other types of renewable energy or clean chemical fuels such as hydrogen [1–5]. In particular, photochemical water splitting, which directly converts solar energy into chemical energy by imitating natural photosynthesis has long existed as the "Holy Grail" of chemists and thus attracted great attention. With the recent discovery of graphene [6, 7], delaminating two-dimensional (2D) layered materials such as hexagonal boron nitride, MoS_2, and WS_2 bulk particles into the corresponding nanosheets has induced intriguing photoelectrochemical properties, including giant charge carrier mobility, high specific surface area, and pronounced changes in the energy band structure [8–12]. Consequently, 2D ultrathin layered semiconductor structures such as nanobelts [13], nanosheets [14–16], and nanoplates [17] have been identified as promising materials for photochemical water splitting owing to the improved charge separation and higher

Address correspondence to Liangti Qu, lqu@bit.edu.cn ; Zhipan Zhang, zhipan@bit.edu.cn

percentage of surface atoms, featuring a vast number of active edge sites that are preferentially desirable in photocatalysis as they could potentially serve as efficient catalytic centers with high catalytic activity. In the past decade, various 2D transition-metal semiconductor nanostructures have been proposed for efficient water splitting under solar illumination [18, 19]. Ultrathin nanosheets of TiO_2 [20, 21] are cost-effective and abundant, but they show a narrow spectral response and are only sensitive to ultraviolet (UV) light, which merely accounts for about 4% of the solar radiation energy. As visible light contributes to about 43% of the total energy in the solar spectrum, researchers have developed photocatalysts responsive to visible light, such as nanoplates of CdS, $Ba_5Ta_4O_{15}$, and Bi_2WO_6 [14, 17, 22]. Unfortunately, CdS is less stable under illumination, and the other compounds show limited hydrogen evolution rates [5, 17, 23]. Therefore, it is of great theoretical and practical importance to search for new photocatalysts with high response to visible-light illumination, for cost-effective hydrogen production.

Recently, the abundant and environmentally benign carbon-based materials have attracted considerable interest as metal-free photocatalysts with high activity and long-term stability. In particular, graphitic carbon nitride (GCN) is a graphite-like 2D layered material with suitable conduction band and valence band levels for generating hydrogen and oxygen under visible-light irradiation [24–26]. There are two reported approaches to delaminate bulk GCN into thinner 2D sheets [27, 28]. The first approach is the thermal oxidation etching of bulk GCN under heating at 500 °C in air [27]. This process affords GCN nanosheets with notably enhanced photocatalytic activity as compared to the corresponding bulk materials due to the improved charge separation and feasibility to tune the band structure; however, the low yield (6 wt%) [27] poses technical challenges and thus hinders mass production. The second method involves liquid-phase exfoliation of bulk GCN, where GCN is suspended in certain solvents and then sonicated for 10 h [28]. For this reason, large quantities of organic solvents (e.g., isopropanol) and requires extensive sonication are required, which in turn render scale up in large-scale production difficult [28]. More importantly, both these methods only yield GCN sheets of more than 6 layers [27, 28]. To the best of our knowledge, there is no report on the preparation of ultrathin graphitic carbon nitrides nanoplatelets (UGCNPs) for use as photocatalysts in visible-light water splitting. Herein, we report a convenient method for the scalable production of UGCNPs via simple and eco-friendly ball milling of pristine bulk GCN. The synthesized UGCNPs feature a uniform diameter of 2 to 6 nm and show strong response in the visible-light region, demonstrating excellent photocatalytic activity in visible-light water splitting.

2 Experimental

Preparation of UGCNPs: UGCNPs were prepared by ball milling the bulk GCN in a planetary ball mill (ND8). The bulk GCN was synthesized by heating melamine at 600 °C in air for 2 h, with a ramp rate of 2.3 °C·min^{-1}. Then, the bulk GCN powder (2.0 g) was placed in a stainless-steel capsule containing stainless-steel balls (200 g, diameter 6 mm). Thereafter, the capsule was fixed in the planetary ball mill and agitated at 500 rpm for 48 h. The resultant product was dispersed in absolute ethanol, and the supernatant fraction was extracted by centrifuging at 5,000 rpm to remove larger particles and subsequently filtered through a 220 nm filter membrane to yield a homogeneous dispersion of UGCNPs. Finally, the suspended solution was freeze-dried at −40 °C under reduced pressure (30 Pa) for 48 h to give 0.3 g of UGCNPs.

Electrochemical measurements: The energy level of the samples was evaluated by cyclic voltammetry (CV) experiments conducted on a CHI660D electrochemical workstation with a traditional three-electrode system. A glassy carbon disk was used as the working electrode; a platinum wire, as the counter electrode; and Ag/AgCl electrode, as the reference. About 4 μL of the sample/chloroform suspensions (5 mg·mL^{-1}) was spun onto the working electrode and dried naturally. A 0.1 M tetrabutylammonium hexafluorophosphate ($TBAPF_6$, Aldrich)/acetonitrile solution was used as the supporting electrolyte in the CV measurements; the electrolyte was purged with high-purity argon gas for 15 min before the measurement. The applied bias range was 0.5–1.7 V vs. Ag/AgCl, and the scan rate was 5 mV·s^{-1}. Electrochemical impedance measurements

were performed on a potentiostat (Autolab, Model 204) with an amplitude of 20.0 mV, over the frequency range 10 kHz–1 Hz under applied biases ranging from –1.5 V to –1.1 V vs. Ag/AgCl, with an interval of 0.1 V.

Photochemical measurements: Transient photocurrent measurements were performed on a Keithley 6,300 semiconductor parameter analyzer under an applied bias of 0.1 V in a conventional three-electrode cell, where a sample-coated clean fluoride-tin oxide (FTO) glass, Pt wire, and a Ag/AgCl electrode were used as the working, counter, and reference electrodes, respectively. An aqueous solution of 0.2 M Na_2SO_4 purged with nitrogen gas was used as the electrolyte.

Photocatalytic water splitting was carried out in a top-irradiation vessel connected to a gas-closed glass system. About 50 mg of photocatalyst powder was dispersed in 100 mL of an aqueous solution containing 10 vol% triethanolamine scavenger and 3 wt% (respect to Pt, acting as the co-catalyst) $H_2PtCl_6{\cdot}6H_2O$. The temperature of the reaction solution was carefully maintained below 6 ℃ during the experiment. The reactor was then sealed and evacuated several times to remove air before irradiation under a 300 W Xe lamp equipped with a 420 nm cutoff filter. The amount of evolved H_2 was analyzed by gas chromatography (GC-7920) using high-purity nitrogen carrier gas. A 350 nm cutoff filter was also used in one experiment to better match the absorption spectrum of UGCNPs. The external quantum yield (Φ) was measured by using an appropriate bandpass filter (365, 420, 475, 500, and 550 nm, respectively) to perform the water splitting experiment under the designated monochromic light. The intensity of the monochromic light was averaged at 5 representative points (CEL-NP 2000 spectroradiometer), and the active area of the reactor was approximately 50.3 cm^2. The external quantum yield was then calculated using Eq. (1):

$$\Phi = \frac{2 \times \text{amount of } H_2 \text{ molecules evovled}}{\text{number of incident photons}} \times 100 \quad (1)$$

The turnover number (TON) was estimated by using Eq. (2):

$$\text{TON} = \frac{\text{moles of } H_2 \text{ molecules evovled}}{\text{moles of platinum on the photocatalyst}} \quad (2)$$

Characterization: The morphology of the samples was examined by transmission electron microscopy (TEM; JEM-2010) and atomic force microscopy (Veeco D3100). X-ray diffraction (XRD) patterns were obtained by using a Netherlands 1,710 diffractometer with a Cu Kα irradiation source (λ = 1.54 Å). Raman spectra were recorded on a Horiba JY HR-800 Raman spectrometer with an excitation wavelength of 785 nm. Fourier transform infrared (FT-IR) spectra were recorded on a Bruker spectrometer (Equinox 55/S) using KBr pellets. X-ray photoelectron spectroscopy (XPS) measurements were performed using an ESCALAB 250 photoelectron spectrometer (ThemoFisher Scientific), with Al Kα (1,486.6 eV) radiation. UV–Vis absorption and photoluminescence spectra were measured with a 5,300pc spectrophotometer and a SPEX flourolog-3 fluorimeter The Brunauer-Emmett-Teller (BET) speci_c surface area was determined by nitrogen adsorption-desorption isotherm measurements at 77 K (NOVA 2200e).

3 Results and discussion

A schematic of the ball-milling-driven exfoliation of the pristine bulk GCN to UGCNPs is shown in Figs. 1(a) and1 (b) (see Experimental Section). Samples of bulk GCN were first prepared by using melamine as the precursors, and UGCNPs were synthesized by a facile ball-milling process. Ball milling can effectively induce the cleavage of C–C bonds, while simultaneously causing doping and exfoliation in graphene [29–32]. Hence it is reasonable to infer that ball milling can be employed to cut and exfoliate GCN, which has a similar 2D layered structure, except that the neighboring layers are held by hydrogen bonding rather than the weak van der Waals force [24, 33, 34]. Therefore, the stainless-steel balls rotating at 500 rpm should generate sufficient energy to cleave the bulk sheets into nanopieces and break the interlayer stacking, to form suspensions of exfoliated GCNs where UGCNPs could be obtained after centrifugation. Intriguingly, the color of GCN turned from yellowish to white after ball milling (Fig. S1 in the Electronic Supplementary Material (ESM)), implying a change in the electronic structure of UGCNPs as compared to that of bulk GCN.

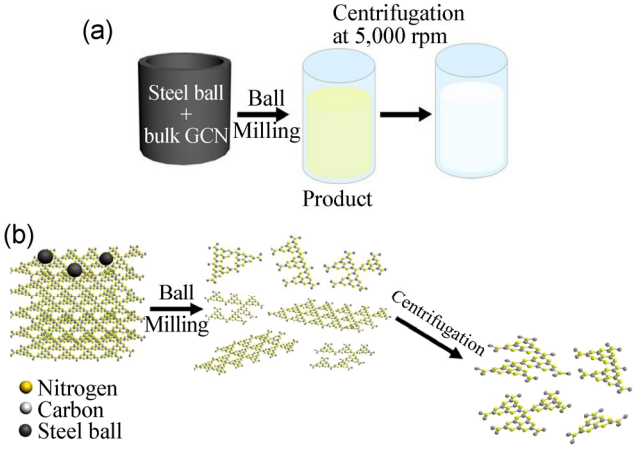

Figure 1 (a) Schematic of the preparation process. (b) Cartoonic illustration of the physical exfoliation of bulk GCN by ball milling to form UGCNPs. Yellow, gray, and black spheres stand for nitrogen atoms, carbon atoms, and steel balls, respectively.

The morphology and microstructure of the UGCNPs were first investigated by TEM and AFM. TEM images in Figs. 2(a) and 2(b) clearly show that the UGCNPs formed after ball milling are homogenous and 2–6 nm in size, much smaller than the GCN sheets synthesized by thermal oxidation etching [27] and liquid-phase exfoliation [28]. Additionally, topological analysis by AFM (Figs. 2(c) and 2(d)) revealed that the UGCNPs have a height of 0.35 to 0.7 nm, suggesting that they mainly consist of less than three layers and approximately 60% of the UGCNPs are single-layered considering that the interlayer distance in GCN is 0.326 nm [24]. Therefore, the TEM and AFM results demonstrated that bulk GCN has been successfully reduced to a few nanometers in size and exfoliated into single or few-layer UGCNPs by the ball milling, with the new surfaces rich in potentially active photocatalytic sites generated *in situ* via the exfoliation and bond cleavage of GCN. The increase in the specific surface area was further confirmed by Brunauer-Emmett-Teller (BET) surface area measurements, from N_2 adsorption-desorption isotherms. As shown in Fig. 2(e), the BET surface area of the UGCNPs was 97 $m^2 \cdot g^{-1}$, which was 9.7-fold greater than that of bulk GCN (10 $m^2 \cdot g^{-1}$). Such a remarkable increase in the specific surface area of UGCNPs is deemed beneficial for their application as photocatalysts, where greater exposure of the interfacial contact to the reactant is highly desired.

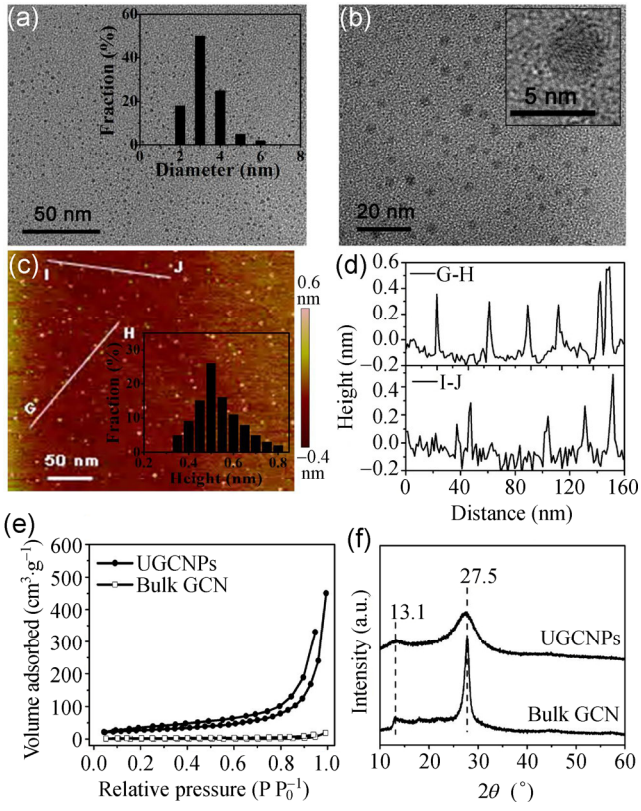

Figure 2 (a, b) TEM images of UGCNPs under different magnifications. (c) AFM image of UGCNPs on the Si substrate. (d) Height profiles along the lines in (c). (e) N_2 adsorption isotherms and (f) XRD patterns of the bulk GCN and UGCNPs. The insets in (b) and (c) show the size and height distributions of UGCNPs. Scale bars are 50, 20, and 50 nm in (a), (b), and (c), respectively.

The UGCNP samples were further characterized by XRD measurements. As presented in Fig. 2(f), both bulk GCN and UGCNPs show two consistent peaks, implying that their basic structure remains unchanged. The low-angle peak at 13.1° originating from the lattice planes parallel to the c-axis [33] becomes less pronounced in the case of the UGCNPs than in the case of bulk GCN, consistent with the decreased planar size of the GCN layers during the physical cracking of bulk GCN [27]. Meanwhile, the strong (002) peak at 27.5°, corresponding to the interlayer stacking of conjugated aromatic systems [35] in pristine bulk GCN, broadens and diminishes in the XRD spectrum of the UGCNPs, signifying that a high degree of exfoliation [27, 28] occurred without lattice expansion during ball milling. As size reduction could generally provide entropic gains for good dispersion [30], the UGCNPs can be homogenously dispersed in various

common solvents such as isopropanol, acetone, dimethylformamide, and water at concentrations of up to 0.1 mg·mL^{-1}, without precipitation even after storage for 1 month under ambient conditions (Fig. S2(a) in the ESM). This effect is in sharp contrast to the poor dispersibility observed in bulk GCN samples (Fig. S2(b) in the ESM). The zeta potential of the UGCNPs and bulk GCN in 0.1 mg·mL^{-1} aqueous solution were measured to be –28.2 mV and –29.4 mV, respectively. This implies that both samples possess a positively charged, acidic surface and that the UGCNPs show less surface protonation, which may lead to an improved hydrogen evolution rate [36].

XPS measurements were employed to accurately determine the surface chemical states of UGCNPs and thus probe their composition. As shown in Fig. 3(a), both UGCNPs and bulk GCN exhibited a typical pronounced C1s peak at ca. 284.8 eV, a N1s peak at ca. 398.6 eV, and a trace O1s peak at ca. 531.8 eV arising from the physically adsorbed oxygen [37]. The N/C atomic ratio was 1.26 for UGCNPs, similar to that of bulk GCN (1.31). The high-resolution N1s spectra of UGCNPs and bulk GCN (Fig. 3(b)) confirmed the presence of sp^2 C–N=C (398.8 eV), N–(C)$_3$, or N bonded with H atoms (399.7 eV) and C–NH$_x$ (amino functional groups, 401 eV), where the small peak at 404.4 eV can be rationally assigned to charging effects, π excitation, or cyano group [37, 38]. The sp^2-bonded nitrogen atom, hybrid sp^3 nitrogen atoms, and amino groups are key features of the GCN structure and surface characteristics, with sp^2 C–N=C bonds particularly contributing to band-gap absorption [37–39]. The UGCNPs possess the same nitrogen species (C–N=C, N–[C]$_3$ and C–NH$_x$) as those of bulk GCN, and the relative percentages of the nitrogen species undergo a mild change (66.49% vs. 62.13% C–N=C, 18.94% vs. 22.67% N–[C]$_3$, and 11.06% vs. 11.21% for C-NH$_x$). The decrease in the case of N–[C]$_3$ of the UGCNPs presumably originates from the breaking of sp^3 N–C bonds during the ball-milling process to exfoliate bulk GCN to smaller and thinner platelets. Therefore, the ratio of sp^2 C–N=C bonds to the sum of sp^3 N–[C]$_3$

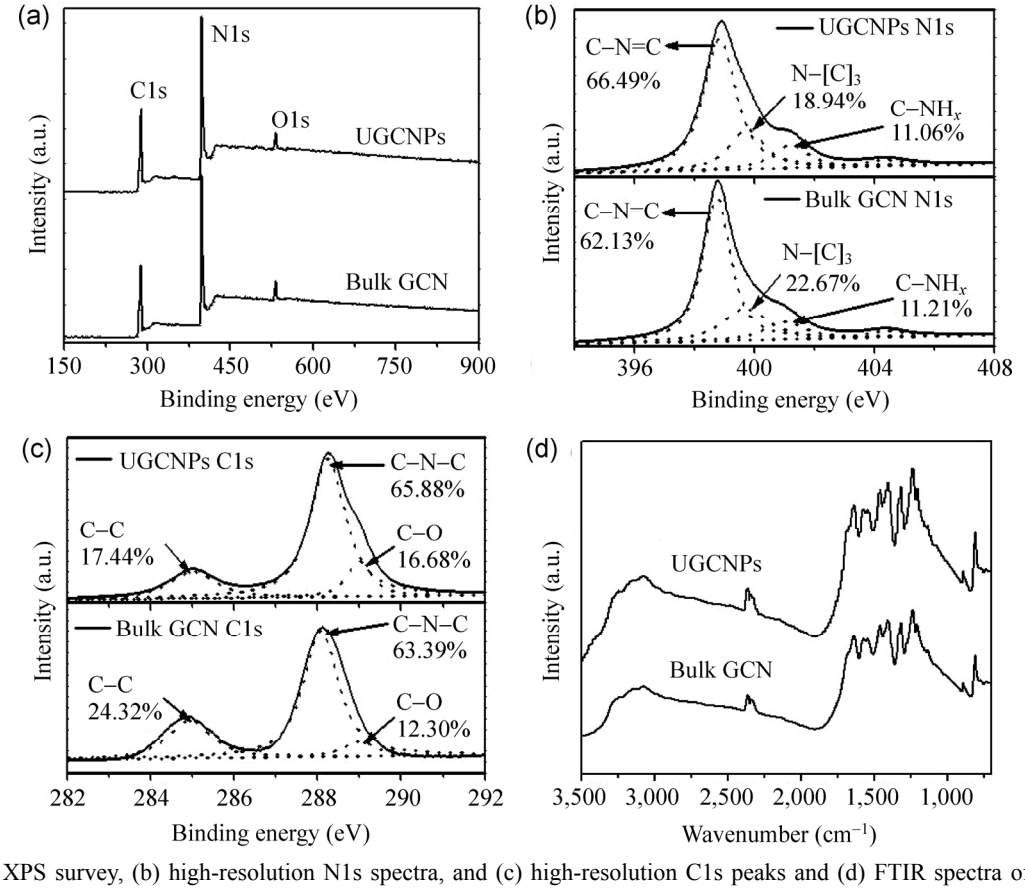

Figure 3 (a) XPS survey, (b) high-resolution N1s spectra, and (c) high-resolution C1s peaks and (d) FTIR spectra of UGCNPs and bulk GCN.

and C–NH_x bonds increases from 1.83 for bulk GCN to 2.22 for UGCNPs; this increased ratio leads to a concomitant decrease in proton concentration (from both sp^3 nitrogen atoms and C-NH_x) [36] in UGCNPs, in agreement with the case of the less protonated surface found in the zeta potential measurements. As suggested by Martin et al. [36], the relative increase in the ratio of sp^2 C–N=C bonds to the sum of sp^3 N–$[C]_3$ and C–NH_x bonds potentially leads to higher hydrogen evolution activity, as is also confirmed in our case (*vide infra*). Meanwhile, similar to that of bulk GCN (Fig. 3(c)), the high-resolution C1s spectrum of UGCNPs can be deconvoluted into three different peaks at binding energies of 285.1 (C–C), 288.2 (C–N–C), and 289.2 eV (C–O). The O1s fittings display two peaks at 532 and 534 eV from N–C–O and adsorbed oxygen [38], respectively (Fig. S3 in the ESM). Consistent with the X-ray photoelectron spectra, the energy-dispersive X-ray (EDX) spectra (Table S1 and Fig. S4(a) in the ESM) demonstrate that UGCNPs have slightly higher oxygen content, presumably because of the reactions of moisture and/or absorbed oxygen with the chemically active carbon or nitrogen species (radicals, anions and cations) generated by the cleavage of the carbon nitride C–N bonds during the ball-milling process. Overall, the UGCNPs show similar surface states with small changes in N1s, C1s, and O1s peaks (Table S1 in the ESM). Additionally, the resemblance of UGCNPs and bulk GCN in the FTIR (Fig. 3(d)) and Raman spectra (Fig. S4 in the ESM) suggests the presence of similar functional groups (see Fig. S4 for detailed assignments of FTIR and Raman spectra). These observations confirm that ball milling is a mild but effective approach to cut bulk GCN sheets and delaminate the thick GCN layers into UGCNPs while retaining the in-plane conjugated structure of the original bulk GCN.

The band structure of the UGCNPs was measured by UV–Vis absorption spectroscopy, photoluminescence (PL) measurements, and CV. Fig. 4(a) shows

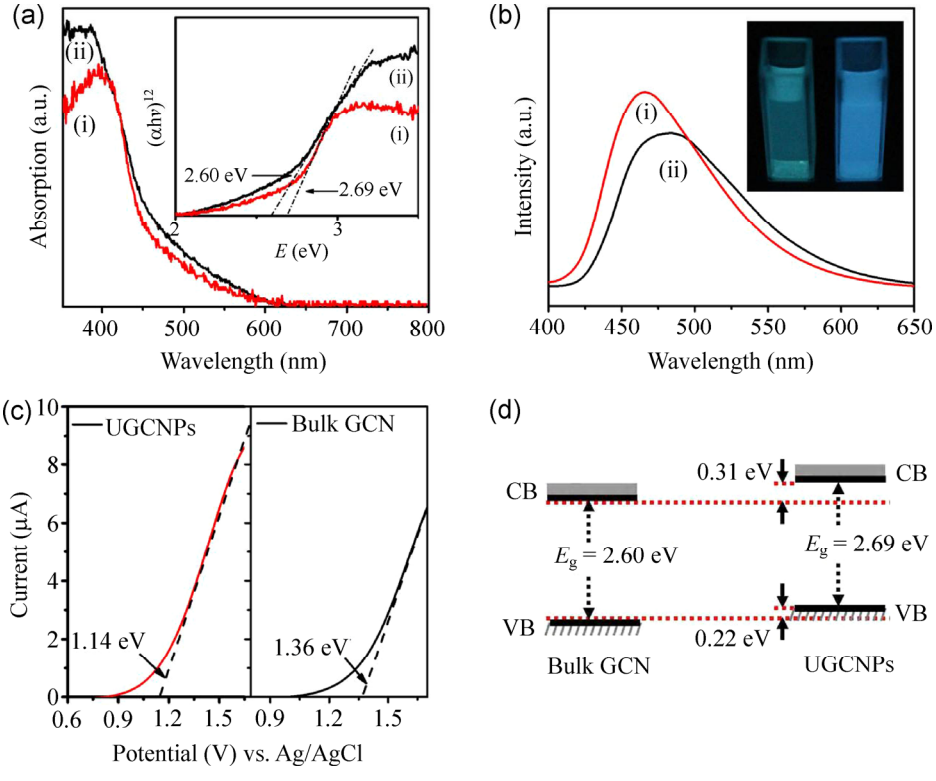

Figure 4 (a) UV-Vis absorption spectra of UGCNPs (i, red curve) and bulk GCN (ii, black curve). The inset shows the plot of $(\alpha E)^{1/2}$ against photon energy (E) for UGCNPs and bulk GCN, where α is the absorbance. (b) PL spectra, with the excitation wavelength of 380 nm. The inset is a photograph of UGCNPs (right) and bulk GCN (left) in water under 365 nm UV irradiation. (c) Anodic scans of 5 $mV \cdot s^{-1}$ showing the valence band maximum (VBM) of UGCNPs and bulk GCN. (d) Schematic illustration of band structures of UGCNPs and bulk GCN.

the typical absorption spectra of the UGCNPs and bulk GCN, where both curves feature a strong absorption extending from the UV region to the visible light region. The absorption spectrum of UGCNPs shows a hypochromic shift as compared to that of bulk GCN, and the absorption maximizes at 420 nm. The bandgaps derived from Tauc's plot (inset of Fig. 4(a)) are 2.69 eV for the UGCNPs and 2.60 eV for bulk GCN. The bandgap of the UGCNPs is widened by 0.09 eV, as is further confirmed by the blueshift of the fluorescence emission peak from 482 to 462 nm in Fig. 4(b). As a result, under 365 nm excitation, the UGCNPs emit intense blue photoluminescence (Fig. 4(b) inset), which is clearly different from the green luminescence of bulk GCN. The larger bandgap and the blueshift in the PL spectrum of the UGCNPs should originate from the decrease in the nanoplatelet size and thickness associated with the quantum confinement effect. A similar effect has been reported by Groenewolt and Antonietti, who attempted to understand such spectral changes in the case of GCN nanoparticles [35]. For determining the band energy levels of the UGCNPs, CV was performed to estimate the valence band maximum (VBM) of both materials (Fig. 4(c)), since anodic currents will abruptly emerge when the scanning potentials move below the VBM [40, 41]. The anodic scan results in Fig. 4(c) clearly show that the VBM of the UGCNPs is raised by 0.22 eV (from 1.36 to 1.14 eV vs. Ag/AgCl), enabling direct comparison of the whole band diagrams between the UGCNPs and the bulk GCN in Fig. 4(d). In allowance of the 0.09 eV increase in the bandgap and a negative shift of 0.22 eV in the VBM, the conduction band minimum (CBM) of the UGCNPs is calculated to be upshifted by 0.31 eV, probably because the surface protonation is lesser than that of bulk GCN, as determined in the zeta potential measurements. Such a large shift in the CBM leads to a larger thermodynamic driving force in photocatalytic reductions such as hydrogen evolution. Therefore, UGCNPs can be an ideal photocatalyst, with abundant surface atoms and better aligned energy levels, in hydrogen evolution driven by visible-light illumination.

The catalytic activity of the UGCNPs and bulk GCN samples were evaluated by the electrochemical impedance spectroscopy (EIS) and hydrogen evolution measurements under visible-light illuminations. Figure 5(a) compares the Nyquist plots of the UGCNPs and bulk GCN obtained in a 0.2 M Na_2SO_4 aqueous solution, under an applied bias of –1.5 V vs. Ag/AgCl in the dark. The symbols represent raw data, and the solid lines represent the fitting curves by the model in the inset. Here, R_s, R_{ct}, and CPE represent the series resistance, charge transfer resistance at the

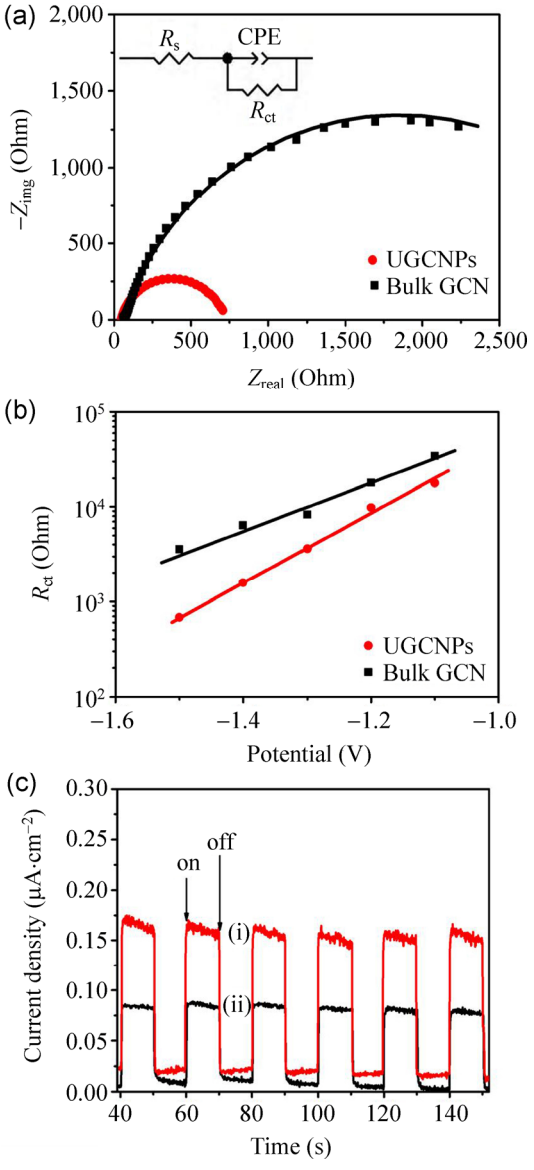

Figure 5 (a) Nyquist plots of UGCNPs (i) and bulk GCN (ii) obtained at a bias of –1.5 V vs. Ag/AgCl. The symbols represent raw data, and the solid lines are the fitting curves by the model in the inset. (b) Dependence of R_{ct} on applied biases in EIS experiments. (c) Transient photocurrents under visible-light illumination ($\lambda > 420$ nm) for UGCNPs (i) and bulk GCN (ii) obtained at 0.1 V vs. Ag/AgCl in a 0.2 M Na_2SO_4 aqueous solution pH 6.8).

solid/electrolyte interface, and the corresponding constant phase element, respectively. The UGCNP sample gives a much smaller semicircle than that of bulk GCN, suggesting that R_{ct} at the UGCNPs/electrolyte interface is significantly decreased and that electrons in the UGCNPs could more readily transferred to the protons from the conduction band of the UGCNPs rather than from the conduction band of bulk GCN [42, 43]. EIS is also performed in the potential range from –1.4 to –1.1 V vs. Ag/AgCl with a 100 mV interval; the fitting results are summarized in Fig. 5(b). In both cases, R_{ct} decreases exponentially with increasing negative bias, as expected from the Butler-Volmer kinetics with a linear increase in the overpotential. Importantly, the UGCNPs feature a smaller R_{ct} than that of bulk GCN at any given bias, suggesting that they are more active in reducing protons into hydrogen. This is also reflected in the transient photocurrent measurements in Fig. 5(c), where the UGCNPs show a plateau current density twice that of bulk GCN under transient visible-light irradiation.

The photocatalytic activity of UGCNPs in visible-light water splitting is presented in Fig. 6(a). When $\lambda > 420$ nm, stable hydrogen evolution catalyzed by the UGCNPs is observed, with an average hydrogen evolution reaction (HER) rate of 1,365 μmol·h^{-1}·g^{-1}, which is 13.7 times that of bulk GCN (99.75 μmol·h^{-1}·g^{-1}), and a turnover number (TON, see Experimental for details) of 36 in 4 h. As listed in Table 1, these values are among the best for reported GCN catalysts in visible-light water splitting under the same conditions, highlighting the efficacy of ball-milling process in producing efficient photocatalysts. The UGCNPs also show high stability, with reproducible hydrogen yields in 3 cycles and up to 12 h. To study the wavelength dependence of photocatalytic activity, the external quantum efficiency of the UGCNPs is measured from 360 to 550 nm (Fig. 6(b)). The quantum efficiency resembles the absorption spectrum, and the value at 420 nm is measured to be 3.5%, which is close to that of the GCN nanosheets reported in Ref. 1 and superior to that of I-doped GCN (Table 1). The HER rate of the

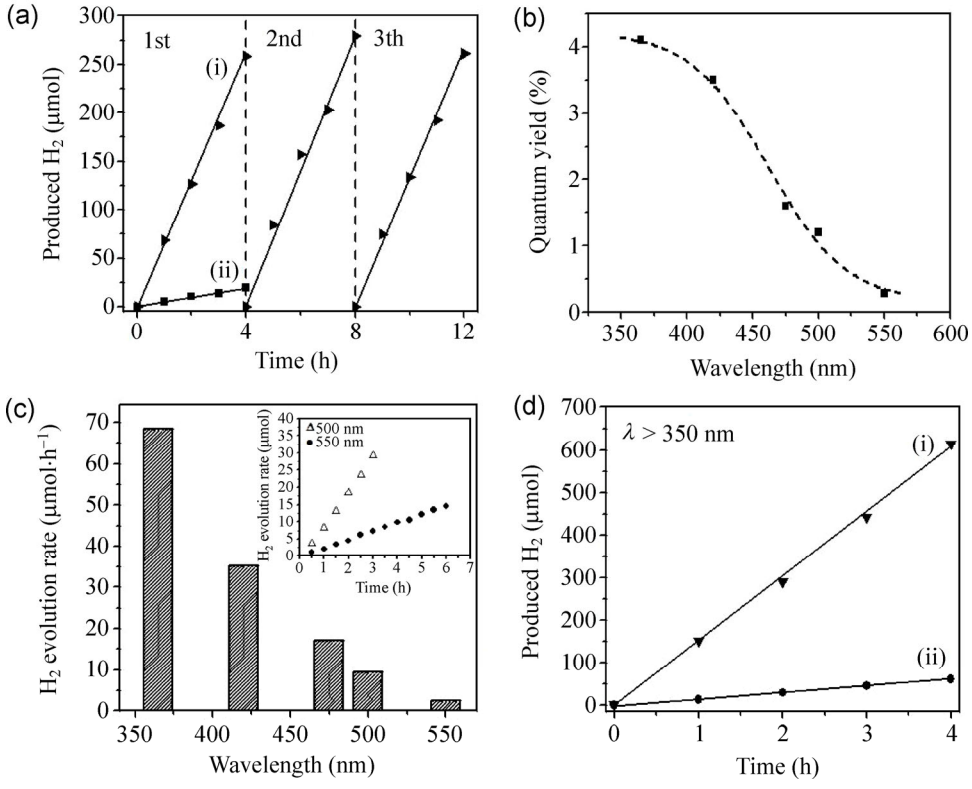

Figure 6 (a) Photocatalytic activities toward H_2 production of UGCNPs (i) and bulk GCN (ii) under $\lambda > 420$. (b) Quantum yield of UGCNPs measured by using band-pass filters at specific wavelengths. (c) Wavelength dependence of H_2 evolution rate for UGCNPs (inset: time-dependent H_2 evolution rate under 500 and 550 nm light irradiation). (d) The amount of H_2 produced in the case of UGCNPs (i) and bulk GCN (ii) under $\lambda > 350$ nm.

Table 1 Comparison of GCN photocatalysts reported for hydrogen production

Photocatalyst[a]	HER rate under visible light ($\mu mol \cdot h^{-1} \cdot g^{-1}$)	Quantum efficiency at 420 nm (%)	Ref.
GCN	106.9	—	[24]
GCN (S-doped)	800	—	[44]
GCN (I-doped)	760	2.4	[45]
GCN nanosheets[1]	1,860	3.75	[28]
GCN nanosheets[2]	650	—	[27]
This work	1,365	3.6	—

[a] All photocatalysts listed were loaded with 3 wt% Pt co-catalyst except GCN (S-doped) and GCN nanosheets[2], which were loaded with 6 wt% Pt co-catalyst.

UGCNPs is further measured under corresponding monochromic light (Fig. 6(c)), and 14.5 μmol H_2 is produced after 6 h of reaction under 550 nm illumination.

It is interesting to note that the catalytic performance of GCN nanosheets in Ref. 1 and 2 is only 3 and 9.3 times higher than their bulk counterparts, while in the current work a 13.7-fold increase has been observed (Table 1). As proposed previously, the pronounced enhancement in the photoreductive water splitting of our ball-milling-derived samples can be explained by the following rationales: (i) It has been reported that carbon atoms provide the reduction sites for reducing H^+ to H_2 [24]. As UGCNPs feature a much reduced sheet size and thickness, the well-improved specific surface area and homogenous dispersion enable them to expose more catalytic carbon atoms working at the g-C_3N_4 catalyst/water interface as the active reduction sites for hydrogen evolution than bulk GCN. (ii) The preservation of the conjugated structure of GCN and the production of more active sites after ball milling; (iii) The less protonated surface after ball-milling leads to better aligned conduction band and valence band levels, which are more favorable for hydrogen evolution without greatly sacrificing the spectral responses. Additionally, the observed 13.7-fold increase in the hydrogen evolution rate of UGCNPs is apparently more significant than the 9.7-fold improvement in the specific surface area, implying that the quantum confinement effect induced by the decreased sheet size and thickness may also lead to a higher photocarrier separation efficiency that is subjected to further investigations. Finally, when a 350 nm cutoff filter was used, stable hydrogen evolution by UGCNPs could improve and become 3,035 $\mu mol \cdot h^{-1} \cdot g^{-1}$ under this illumination (Fig. 6(d)), further demonstrating the potential of UGCNPs as an efficient catalyst in photocatalytic water splitting.

In conclusion, we have developed a simple but effective ball-milling approach for producing ultrathin GCN nanoplatelets, which show unique optoelectronic features different from those of bulk GCN counterparts. The ball-milled nanosheets show improved electron transfer ability and have better aligned energy levels than those of bulk GCN for photocatalytic water splitting, thereby significantly improving the hydrogen evolution rates under visible light. Apart from using UGCNPs as a photocatalyst for hydrogen evolution, its unique photoluminescence could also be exploited in optoelectronic devices and biological applications such as bio-imaging, bio-labeling, and light-emitting diodes and many other potential applications.

Acknowledgements

This project is sponsored by NSFC (Nos. 21325415, 21174019, 21301018, 51161120361), National Basic Research Program of China (2011CB013000), Basic Research Foundation of Beijing Institute of Technology (20121942008), Fok Ying Tong Education Foundation (No. 131043), the 111 Project B07012, Beijing Natural Science Foundation (2152028) and the Beijing Key Laboratory for Chemical Power Source and Green Catalysis under the contract no. 2013CX02031.

Electronic Supplementary Material: This material is available in the online version of this article at http://dx.doi.org/10.1007/s12274-014-0675-9.

References

[1] Kim, Y. I.; Salim, S.; Huq, M. J.; Mallouk, T. E. Visible-light photolysis of hydrogen iodide using sensitized layered semiconductor particles. *J. Am. Chem. Soc.* **1991**, *113*, 9561–9563.

[2] Hoffmann, M. R.; Martin, S. T.; Choi, W. Y.; Bahnemann, D. W. Environmental applications of semiconductor photocatalysis. *Chem Rev.* **1995**, *95*, 69–96.

[3] Grätzel, M. Photoelectrochemical cells. *Nature.* **2001**, *414*, 338–344.

[4] Maeda, K.; Teramura, K.; Lu, D. L.; Takata, T.; Saito, N.; Ioune, Y.; Domen, K. Photocatalyst releasing hydrogen from water. *Nature.* **2006**, *440*, 295.

[5] Chen, X. B.; Shen, S. H.; Guo, L. J.; Mao, S. S. Semiconductor-based photocatalytic hydrogen generation. *Chem Rev*. **2010**, *110*, 6503–6570.

[6] Novoselov, K. S.; Geim, A. K.; Morozov, S. V.; Jiang, D.; Zhang, Y.; Dubonos, S. V.; Grigorieva, I. V.; Firsov, A. A. Electric field effect in atomically thin carbon films. *Science*. **2004**, *306*, 666–669.

[7] Janowska, I.; Chizari, K.; Ersen, O.; Zafeiratos, S.; Soubane, D.; Costa, V. D.; Speisser, V.; Boeglin, C.; Houllé, M.; Bégin, D.; et al. Microwave synthesis of large few-layer graphene sheets in aqueous solution of ammonia. *Nano. Res.* 2010, 3, 126–137.

[8] Zhou, H. Q.; Zhu, J. X.; Liu, Z.; Yan, Z.; Fan, X. J.; Lin, J.; Wang, G.; Yan, Q. Y.; Yu, T.; Ajayan, P.; et al. High thermal conductivity of suspended few-layer hexagonal boron nitride sheets. *Nano. Res.* 2014, 7, 1232–1240.

[9] Jaramillo, T. F.; Jørgensen, K. P.; Bonde, J.; Nielsen, J. H.; Horch, S.; Chorkendorff, I. Identigication of active edge sites for electrochemical H_2 evolution from MoS_2 nanocatalysts. *Science.***2007**, *317*, 100–102.

[10] Coleman, J. N.; Lotya, M.; O'Neill, A.; Bergin, S. D.; King, P. J.; Khan, U.; Young, K.; Gaucher, A.; De, S.; Smith, R. J.; et al. Two-dimensional nanosheets produced by liquid exfoliation of layered materials. *Science.***2011**, *331*, 568–571.

[11] Zhou, K. G.; Mao, N. N.; Wang, H. X.; Peng. Y.; Zhang, H. L. A mixed-solvent strategyfor efficient exfoliation of inorganic graphene analogues. *Angew. Chem. Int. Ed.* **2011**, *50*, 10839–10842.

[12] Zhou, M.; Lou, X. W. (David); Xie, Y. Two-dimensional nanosheets for photoelectrochemical water splitting: Possibilities and opportunities. Nano Today. **2013**, *8*, 598–618.

[13] Wang, W. W.; Zhu, Y. J.; Yang, L. X. ZnO-SnO_2 hollow spheres and hierarchical nanosheets: Hydrothermal preparation, formation mechanism, and photocatalytic properties *Adv. Funct. Mater.* **2007**, *17*, 59–64.

[14] Xu, T. G.; Zhang, C.; Shao, X.; Wu, K.; Zhu, Y. F. Monomolecular-layer $Ba_5Ta_4O_{15}$ nanosheets: Synthesis and investigation of photocatalytic properties. *Adv. Funct. Mater.* **2006**, *16*, 1599–1607.

[15] Kim, J. Y.; Hiramatsu, H.; Osterloh, F. E. Planar polarized light emission from CdSe nanoparticle clusters. *J. Am. Chem. Soc*. **2005**, *127*, 15556–15561.

[16] Kim, J. Y.; Osterloh, F. E. Planar gold nanoparticle clusters as microscale mirrors. *J. Am. Chem. Soc.* **2006**, *128*, 3868–3869.

[17] Zhang, C.; Zhu, Y. F. Synthesis of square Bi_2WO_6nanoplates as high-activity visible-light-driven photocatalysts. *Chem. Mater*. **2005**, *17*, 3537–3545.

[18] Lu, H. B.; Wang, S. M.; Zhao, L.; Li, J. C.; Dong, B. H.; Xu, Z. X.Hierarchical ZnO microarchitectures assembled by ultrathin nanosheets: hydrothermal synthesis and enhanced photocatalytic activity. *J. Mater. Chem.***2011**, *21*, 4228–4234.

[19] Zhang, X. D.; Xie, X.; Wang, H.; Zhang, J. J.; Pan, B. C.; Xie, Y. Enhanced photoresponsive ultrathin graphitic-phase C_3N_4 nanosheets for biomaging. *J. Am. Chem. Soc.* **2013**, *135*, 18–21.

[20] Liu, G.; Yang, H. G.; Wang, X. W.; Cheng, L. N.; Pan, J.; Lu, G. Q.; Cheng, H. M. Visible light responsive nitrogen doped anatase TiO_2 sheets with dominant {001} facets derived from TiN. *J. Am. Chem. Soc*. **2009**, *131*, 12868–12869.

[21] Liu, G.; Wang, L. Z.; Sun, C. H.; Chen, Z. G.; Yan, X. X.; Cheng, L. N.; Cheng, H. M.; Lu, G. Q. Nitrogen-doped titania nanosheets towards visible light response. *Chem. Comm*. **2009**, 1383–1385.

[22] Qi, L. M.; Colfen, H.; Antonietti, M. Synthesis and characterization of CdS nanoparticles stabilized by double-hydrophilic block copolymers. *Nano. Lett*. **2001**, *1*, 61–65.

[23] Reber, J. F.; Rusek, M. Photochemical Hydrogen-Production with Platinized Suspensions of Cadmium-Sulfide and Cadmium Zinc-Sulfide Modified by Silver Sulfide. *J. Phys. Chem.* **1986**, *90*, 824–824.

[24] Wang, X. C.; Maeda, K.; Thomas, A.; Takanabe, K.; Xin, G.; Carlsson, J. M.; Domen, K.; Antonietti, M. A metal-free polymeric photocatalyst for hydrogen production from water under visible light. *Nat. Mater.* **2008**, *8*, 76–80.

[25] Wang, X. C.; Maeda, K.; Chen, X. F.; Takanabe, K.; Domen, K.; Hou, Y. D.; Fu, X. Z.; Antonietti, M. Polymer semiconductors for artificial photosynthesis: Hydrogen evolution by mesoporousgraphitic carbon nitride with visible light. *J. Am. Chem. Soc*. **2009**, *131*, 1680–1681.

[26] Wang, Y.; Wang, X. C.; Antonietti, M. Polymeric graphitic carbon nitride as a heterogeneous organocatalyst: From photochemistry to multipurpose catalysis to sustainable chemistry. *Angew. Chem. Int. Edit*. **2012**, *51*, 68–89.

[27] Niu, P.; Zhang, L. L.; Liu, G.; Cheng, H. M. Graphene-like carbon nitride nanosheets for improved photocatalyticactivities. *Adv. Funct. Mater*. **2012**, *22*, 4763–4770.

[28] Yang, S. B.; Gong, Y. J.; Zhang, J. S.; Zhan, L.; Ma, L. L.; Fang, Z. Y.; Vajtai, R.; Wang, X. C.; Ajayan, P. M. Exfoliated graphitic carbon nitride nanosheets as efficient catalysts for hydrogen evolution under visible light. *Adv. Mater*. **2013**, *25*, 2452–2456.

[29] Chang, D. W.; Lee, E. K.; Park, E. Y.; Yu, H.; Choi, H. J.; Jeon, I. Y.; Sohn, G. J.; Shin, D.; Park, N.; Oh, J. H.; Dai, L.

M.; Baek, J. B. Nitrogen-Doped Graphene Nanoplatelets from Simple Solution Edge-Functionalization for n-Type Field-Effect Transistors. *J. Am. Chem. Soc.* **2013**, *135*, 8981–8988.

[30] Chang, D. W.; Choi, H. J.; Jeon, I. Y.; Baek, J. B. Edge-selectively functionalized graphene nanoplatelets. *Chem. Rec.* **2013**, *13*, 224–238.

[31] Jeon, I. Y.; Choi, H. J.; Jung, S. M.; Seo, J. M.; Kim, M. J.; Dai, L. M.; Baek, J. B. Large-scale production of edge-selectively functionalized graphene nanoplatelets via ball milling and their use as metal-free electrocatalysts for oxygen reduction reaction. *J. Am. Chem. Soc.* **2013**, *135*, 1386–1393.

[32] Jeon, I. Y.; Zhang, S.; Zhang, L. P.; Choi, H. J.; Seo, J. M.; Xia, Z. H.; Dai, L. M.; Baek, J. B. Edge-selectively sulfurized graphene nanoplatelets as efficient metal-free electrocatalysts for oxygen reduction reaction: The electron spin effect. *Adv. Mater.* **2013**, *25*, 6138–6145.

[33] Lotsch, B. V.; Döblinger, M.; Sehnert, J.; Seyfarth, L.; Senker, J.; Oeckler, O.; Schnick, W.Unmasking melon by a complementary approach employing electron diffraction, solid-state NMR spectroscopy, and theoretical calculations—structural characterization of a carbon nitride polymer. *Chem. Eur. J.* **2007**, *13*, 4969–4980.

[34] Jun, Y. S.; Hong, W. H.; Antonietti, M.; Thomas, A. Mesoporous, 2D hexagonal carbon nitride and titanium nitride/carbon composites. *Adv. Mater.* **2009**, *21*, 4270–4274.

[35] Groenewolt, M.; Antonietti, M. Synthesis of g-C3N4 nanoparticles in mesoporous silica host matrices. *Adv. Mater.* **2005**, *17*, 1789–1792.

[36] Martin, D. J.; Qiu, K. P.; Shevlin, S. A.; Handoko, A. D.; Chen, X. W.; Guo, Z. X.; Tang, J. W. Highly efficient photocatalytic H_2 evolution from water using visible light and structure-controlled graphitic carbon nitride. *Angew. Chem. Int. Edit.* **2014**, *53*, 9240–9245.

[37] Thomas, A.; Fischer, A.; Goettmann, F.; Antonietti, M.; Müller, J. O.; Schlögl, R.; Carlsson, J. M. Graphitic carbon nitride materials: variation of structure and morphology and their use as metal-free catalysts. *J. Mater. Chem.* **2008**, *18*, 4893–4908.

[38] Li, J.; Shen, B.; Hong, Z.; Lin, B.; Gao, B.; Chen, Y. A facile approach to synthesize novel oxygen-doped g-C_3N_4 with superior visible light photoreactivity. *Chem. Commun.* **2012**, 48, 12017–12019.

[39] Cui, Y. J.; Ding, Z. X; Fu, X. Z; Wang, X. C. Construction of conjugated carbon nitride nanoarchitectures in solution at low temperatures for photoredox catalysis. *Angew. Chem. Int. Ed.* **2012**, *51*, 11814–11818.

[40] Peng, Q.; Park, K; Lin, T.; Durstock, M.; Dai, L. Donor-π-acceptor conjugated copolymers for photovoltaic applications: Tuning the open-circuit voltage by adjusting the donor/acceptor ratio. *J. Phys. Chem. B.* **2008**, *112*, 2801–2808.

[41] Yeh, T. F.; Teng, C. Y.; Chen, S. J.; Teng, H. S. Nitrogen-doped graphene oxide quantum dots as photocatalysts for overall water-splitting under visible light illumination. *Adv. Mater.* **2014**, *26*, 3297–3303.

[42] Zhang, J. S.; Chen, X. F.; Takanabe, K.; Maeda, K.; Domen, K.; Epping, J. D.; Fu, X. Z.; Antonietti, M.; Wang, X. C. Synthesis of a carbon nitride structure for visible-light catalysis by copolymerization. *Angew. Chem. Int. Edit.* **2010**, *49*, 441–444.

[43] Zhang, G. G.; Zhang, J. S.; Zhang, M. W.; Wang, X. C. Polycondensation of thiourea into carbon nitride semiconductors as visible light photocatalysts. *J. Mater. Chem.* **2012**, *22*, 8083–8091.

[44] Liu, G.; Niu, P.; Sun, C. H.; Smith, S. C.; Chen, Z. G.; Lu, G. Q.; Cheng, H. M. Unique electronic structure induced high photoreactivity of sulfur-doped graphitic C_3N_4. *J. Am. Chem. Soc.* **2010**, *132*, 11642–11648.

[45] Zhang, G. G.; Zhang, M. W.; Ye, X. X.; Qiu, X. Q.; Lin, S.; Wang, X. C. Iodine modified carbon nitride semiconductors as visible light photocatalysts for hydrogen evolution. *Adv. Mater.* **2014**, *26*, 805–809.